ACS Catalysis

pubs.acs.org/acscatalysis Research Article

# Hydrogen Evolution on Restructured B-Rich WB: Metastable Surface States and Isolated Active Sites

Zisheng Zhang, Zhi-Hao Cui, Elisa Jimenez-Izal, Philippe Sautet, and Anastassia N. Alexandrova*

Cite This: https://dx.doi.org/10.1021/acscatal.0c03410 Read Online

ACCESS | Metrics & More | Article Recommendations | Supporting Information

**ABSTRACT:** Borides have been recently identified to be a class of earth-abundant and low-cost materials that are surprisingly active toward oxidative dehydrogenation and hydrogen evolution reaction (HER) catalysis. Here, we explain from first-principles calculations the HER activity of WB, an industrial material known for its superior physical properties and chemical inertness. We find that, compared to bulk termination, a major surface reconstruction takes place, leading to the off-stoichiometric B-rich surface termination that contains the active sites. The hydrogen adsorbate configurations are further investigated under various adsorbate coverages. Many competing configurations appear to be accessible in reaction conditions, and thus, a grand canonical ensemble is established to describe the catalytic system. A phase diagram of adsorbate coverages is constructed as a function of pH and the applied potential. A complex reaction network is presented based on the ensemble-averaged reaction rates, and the electrocatalytic activities are evaluated under different overpotentials. The major contributors to the activity are found to be a few metastable surface states with a distinct electronic structure that are only accessible at high adsorbate coverages in reaction conditions. In addition, while the activity of the dominant active site is nearly the same as that on the unreconstructed WB, the B-rich formations play an important role of isolating the active sites and preventing the passivation of the surface with $H_2$ bubble formation.

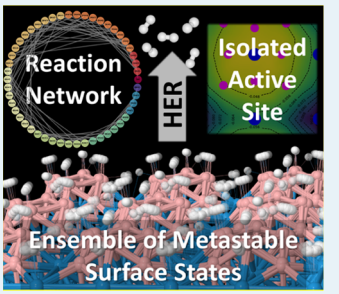


**KEYWORDS:** *hydrogen evolution reaction, tungsten boride, surface restructuring, adsorption configuration*

## INTRODUCTION

The development of inexpensive and noble-metal-free catalysts for energy and environmental applications is increasingly desirable. Transition metal compounds have recently emerged as a family of promising low-cost electrocatalysts with earth-abundant compositions and satisfactory activities, including transition metal phosphides, sulfides, carbides, selenides, and borides.[1,2] Among the large family of compounds, borides have been the less studied while perhaps the most intriguing, due to the rich chemistry of boron (both covalent and delocalized and nondirectional bonds, structural diversity).[3−5] A group of transition metal borides, including those of cobalt,[6] nickel,[7] molybdenum,[8] vanadium,[9] and tungsten,[10] has been identified as active electrocatalysts for the hydrogen evolution reaction (HER) with a high-current density and long-term stability.

Tungsten borides have earth-abundant compositions and are known for their mechanical hardness and thermal/electrical properties.[11,12] Tungsten borides with varying stoichiometries, including $W_2B$, $W_2B_5$, and $WB_4$, have been synthesized by a solid reaction between tungsten and amorphous boron powders.[13,14] Among these tungsten borides, WB was found to exist in a single crystalline phase, and the crystallinity was found to be enhanced with increasing both the time and the temperature of heat treatment.[14] WB crystallizes in either an orthorhombic high-temperature phase or a tetragonal low-temperature phase. The latter is stable up to 2170 °C, when the phase transition occurs. The low-temperature tetragonal phase is an ultra-incompressible material[15] with a bulk modulus of 428−452 GPa,[16,17] and characterized as superconducting below 4.3 K.[18] This phase is composed of boron chains that alternate to form perpendicular arrays. Thanks to the outstanding mechanical and physical properties of WB, together with its chemical inertness, WB has been widely applied in industry for cutting tools and coatings. Thus, it came as a surprise that tungsten borides should be so active toward electrocatalytic HER.

Recent findings point out the likely common structural feature of boride surfaces: the presence of excess boron. First, it is generally known that boride synthesis requires a large off-stoichiometric excess of boron. Borides of many transition metals and also hexagonal boron nitride show analogous selectivities toward propane oxidative dehydrogenation (ODH),[19,20] which was attributed to the partially oxidized amorphous boron layer that forms on their surfaces *in situ* in oxidizing conditions, and restructures on a timescale of picoseconds.[21,22] Additionally, we found that boron-rich structures and monolayers can form on the tungsten metal,

Received: August 5, 2020
Revised: September 26, 2020





https://dx.doi.org/10.1021/acscatal.0c03410
ACS Catal. XXXX, XXX, XXX−XXX

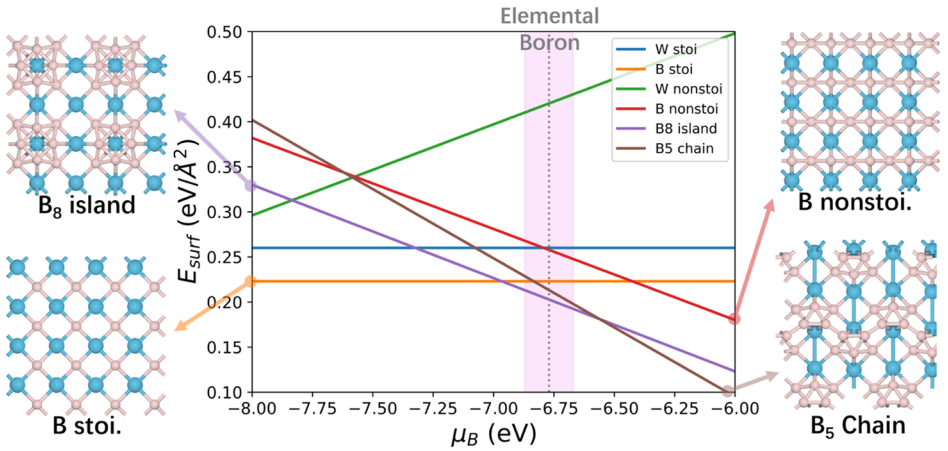


**Figure 1.** Surface energy of W stoichiometric, B stoichiometric, W nonstoichiometric, B nonstoichiometric, $B_8$ island, and $B_5$ chain terminations under different $\mu_B$s, with optimized geometries of the surfaces of interest shown on the left and the right side of the plot. The $\mu_B$ of elemental boron is marked by a dotted line, and the region around it is highlighted with a violet shade. Color code: B (pink) and W (blue).

with the restructuring unlocking novel electronic properties of boron.[23] Encouraged by these studies, we combine global optimization techniques and density functional theory (DFT) to explore the structural diversity of the WB (001) surface with different coverages of excess boron. By calculating the surface energies of the bare WB surfaces with different terminations and the B-excess surfaces with different stoichiometries as functions of the chemical potential of boron, we estimate their relative stabilities, and propose a B-rich WB surface as the actual present phase. To assess the activity of HER, the configurations for H adsorbates on this B-rich surface under different H coverages are then explored, to construct a grand canonical ensemble where the population of each surface state changes as a function of the chemical potential of H. By including potential-dependent and pH-dependent terms into the chemical potential of H, the population of each surface state and the ensemble-averaged reactivity can be evaluated under various reaction electrocatalytic conditions. We demonstrate that it is crucial to account for surface restructuring and multiple accessible adsorption configurations under a grand canonical scheme to properly describe the catalytic interface under realistic conditions.

## RESULTS AND DISCUSSION

To determine the most stable surface terminations of WB, we explored all of the possible low-index surfaces with different terminations and calculated their surface energies. Specifically, we characterized the (100), (110), (201), (210), and (310) surfaces, as well as the (001), (101), and (111) surfaces with both B and W terminations, and the results are summarized in Table S1. It can be seen that the B-terminated surfaces are generally more stable. This scenario is similar to oxide surfaces, where the more electronegative oxygen is more likely to be exposed, though electronegativities of W and B are much closer than those of metals and O. Note that several terminations, such as B-(001) (Y = 3.59 J/m$^2$) and (111) (Y = 3.23 J/m$^2$), have surface energies similar to those of other superhard materials, such as diamond (Y = 3.76 J/m$^2$) and $ReB_2$ (Y = 3.00 J/m$^2$).[24,25] Judging from the calculated surface energies, only the B-terminated (111) and (001) surfaces will be exposed, while the contribution from other surface terminations would be minor and can be neglected.

Because of the large unit cell of the (111) facet and the exponentially growing computational cost of global optimization with increasing cell size, we focused on the (001) facet and thoroughly explored its different nonstoichiometric terminations. A conclusion that will eventually emerge in this study is that similar structural and electronic effects responsible for catalysis are expected to occur on other terminations as well. First, the (001) surface can be cut using four different terminations, including two stoichiometric structures (W terminated W-(001) and B-terminated B-(001) surfaces) and two nonstoichiometric ones (W-rich and B-rich (001)). Second, in addition to these ideal cuts, we explored a wider variety of possible terminations using the particle-swarm optimization (PSO) algorithm combined with the density functional theory (DFT) calculation by varying the number of surface B atoms per unit cell from 0 to a maximum of 8.

The surface energy of the global minimum (GM) termination of each composition under varying chemical potentials of B ($\mu_B$) is shown in Figure 1 (lower surface energy corresponds to higher stability). At the lower limit of $\mu_B$, the B-terminated stoichiometric surface is more stable than the B-rich ones. As the values of $\mu_B$ increases, the thermodynamically most stable state shifts from the stoichiometric terminations to the B-rich terminations. Because experimentally transition metal borides are synthesized by reacting the metal with elemental boron in the powder form, the $\mu_B$ in synthetic conditions should be that of elemental boron. Therefore, the region around the $\mu_B$ of elemental boron would be the most chemically relevant to the realistic termination of the WB surface (highlighted region in Figure 1), and the actual (100) surface structure present in WB is hence predicted to be the B-rich surface with hexagonal island-like $B_8$ clusters. Note that the shape and size of the cluster may change if a larger unit cell would be used in global optimization. However, a likely general qualitative conclusion can be made that boron forms islands on the surface, and some nearly isolated W atoms or rows of W atoms remain exposed at the relevant $\mu_B$.

The binding energies of typical adsorbates that are common in heterogeneous catalysis and electrocatalysis on the bare WB (001) and $B_8$-decorated WB (001) are calculated and summarized in Table S2. The presence of the $B_8$ island not only alters the adsorption values on original sites but also introduces new binding sites. The binding energy of H on the


https://dx.doi.org/10.1021/acscatal.0c03410
ACS Catal. XXXX, XXX, XXX−XXX

$B_8$ island is comparable to that of Pt, which, although is a crude estimation, motivated us to further investigate the surface chemistry of the $B_8$-decorated WB (001) under the HER conditions. The restructured surface has a more complex structure compared to the original WB surface; hence, it is expected to provide multiple kinds of new H adsorption sites. To explore all of the chemically relevant adsorbate configurations on the $B_8$-decorated surface, we exhaustively sampled the adsorbate configurations with the coverage of 1−8 H atoms per unit cell to obtain all of the accessible minima. Figure S1 and Table S3 summarize the energies and geometries of the found surface states. The surface structures are referred to as *m*H#*n*, where *m* is the coverage of adsorbates (number of H's per unit cell) while *n* means it is the *n*th minimum (#1 stands for global minimum) within the *m*H coverage. Note that the upper limit of 8 H per unit cell is chosen because the 8H surface cannot uptake any more H without disintegration of the $B_8$ unit, and such configurations are energetically unstable.

We find that there are several low-energy minima (within 0.5 eV from GM) at each coverage at room temperature, and there are essentially four distinct adsorption sites: top-layer B, sub-layer B, type-1 W, and type-2 W (Figure 2a). Top-layer B is the feature site of the $B_8$-island surface; each such B forms a 4-member ring with the other 3 top-layer B atoms while also bonded to two buried W atoms and two sub-layer B atoms. Note that the top-layer B contains two kinds of sites that differ in the underlying atoms (B or W), but their energetics shows a minor difference (~0.1 eV) and has a similar trend as the coverage increases, so we merge them in this classification. These sub-layer B atoms are in a similar location as the surface B in the stoichiometric surface. Such a unit can host a H adsorbate in a bridging manner under higher coverages. Type-1 W is the surface W site that is more exposed, i.e., not being covered by or directly bonded to the top-layer B atoms. It can bind H in a similar atop position as does the surface W in the stoichiometric surface (Figure S2), and it can bind up to two H atoms under a higher coverage. Type-2 W atoms are less exposed compared to type-1 W atoms, and the H adsorbate on it tends to bridge between the type-2 W and the neighboring top-layer B. Each type of site is labeled on the structural model in Figure 2a.

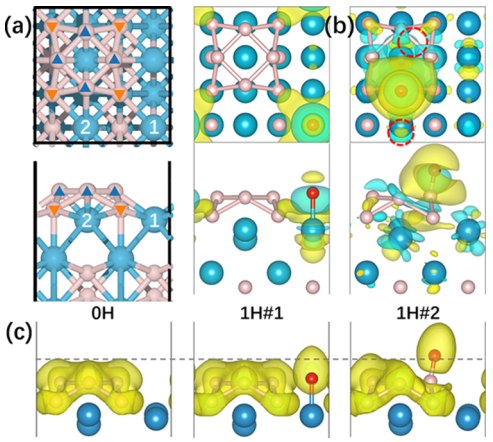


**Figure 2.** (a) Optimized geometry of the WB (001)-$B_8$ island structure from the top and side views, with top-layer B, sub-layer B, type-1, and type-2 W atoms marked with blue triangles, orange inverted triangles, and numbers "1" and "2", respectively. (b) The electron density difference map of H adsorption on W or B sites of the $B_8$-decorated surface at an isovalue = 0.0015, with blue and yellow isosurfaces representing an increase and decrease in the electron density, respectively. (c) The electron localization function plot of 0H, 1H#1, and 1H#2 surface states at an isovalue = 0.475. Color code: H (red), B (pink), and W (blue).

At the 1H coverage, the global minimum (GM) structure 1H#1 has H adsorbed on type-1 W, which is consistent with the stoichiometric surface case, where H is also on W in the GM structure. When the H coverage is increased, surprisingly, the type-1 W is no longer the preferred adsorption site. In 2H#1, 3H#1, and 4H#1, all H atoms are adsorbed on top-layer B, while the configurations with H on type-1 W are the less stable second or the third local minima. Not until the coverage reaches 5H does the GM begin to contain again 1 H on type-1 W.

To investigate the reason for such changes in the adsorption behavior upon increasing the coverage, the electron density difference of H adsorption on top-layer B and type-1 W are calculated. In Figure 2b, it can be seen that, upon H adsorption on type-1 W, the electron density over W and its surrounding sub-layer Bs are reduced, while the region around the W−H bond increases. This can be attributed to the electron transfer from the W−B bonding orbitals to the W−H$\sigma$ orbital. Note that this electron transfer is highly localized, with the electron density of the sub-layer Bs going through a minor decrease and the top-layer Bs being unchanged. In 1H#2, however, a much more significant and delocalized electron transfer can be observed. The electron density over the adsorption site and its neighboring B atoms suffers substantial depletion. From the electron localization function (ELF)[26] plot in Figure 2c, we see that the $B_8$ island is held together by a strong conjugation formed via the overlap of both $\pi$- and $\sigma$-bonds between them (a known bonding phenomenon for boron clusters).[4] Such conjugation is almost unaffected upon H adsorption on type-1 W, but it is broken when the H goes onto the top-layer B site. The weakening of the conjugation system can also be evidenced by lengthening of the B−B bonds as the number of H on top-layer B sites increases from 0H to 4H, as is shown in Figure 3a. Surprisingly, upon the weakening of the conjugation near the adsorption site, the electron density increased on the other side of the top-layer B sites, which are "freed" from the conjugation. As a result, the neighboring top-layer B sites would be "activated" to bind the next adsorbate stronger, and that explains why the top-layer B sites become more favorable at a higher coverage than the W sites. Such a change in the electronic structure can be evidenced by the increase of electron density in the circled region in Figure 2b and the expansion of the ELF isosurface beyond the original one (marked by a gray line in Figure 2c). The emerging electron-rich region between the top-layer B sites on the other side gives rise to the bridging adsorption site over three B atoms in 2H#6. The type-2 W next to the adsorption site is also freed from the conjugation system, and the electron density increases on the other side, leading to the formation of a bridging adsorption site between a type-2 W and a top-layer B. Since the conjugated system is broken as the $B_8$ island gets hydrogenated, the structural stability of the $B_8$ island under H coverage could be questioned. Therefore, Born−Oppenheimer molecular dynamics (BOMD) simulation of the 3H#1 surface state, whose $B_8$ island is partially covered by H, is performed at an elevated temperature of 500 K (Figure S3). The structure of partially covered $B_8$ stays rather stable during the simulation,


https://dx.doi.org/10.1021/acscatal.0c03410
ACS Catal. XXXX, XXX, XXX−XXX

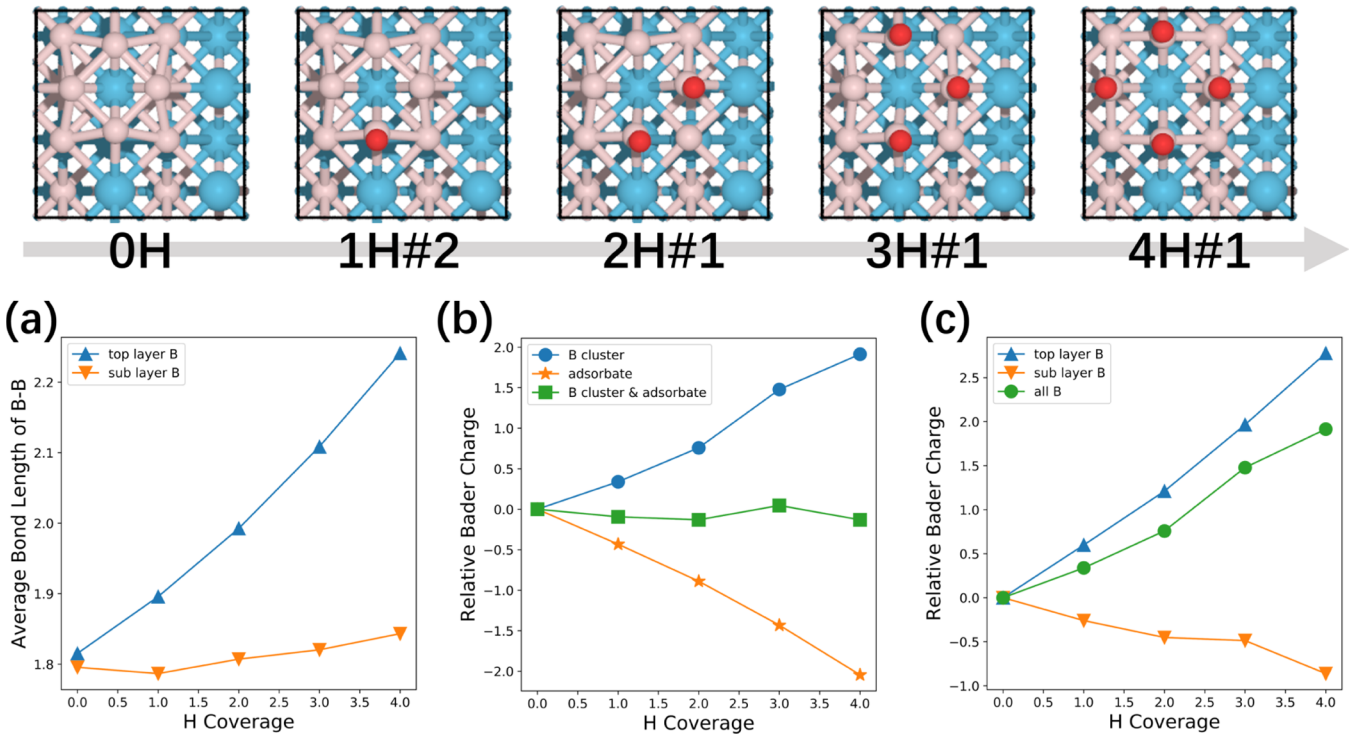


**Figure 3.** (a) Bond length versus number of H plots of the top-layer B−B and sub-layer B−B and the calculated average Bader charge values of (b) B island, adsorbate, and B island with adsorbate, and (c) top-layer, sub-layer, and all surface Bs for featured surface state coverages from 0H to 5H. The optimized geometries of the selected surface states are shown above the plots. Color code: H (red), B (pink), and W (blue).

with the root-mean-square deviation (RMSD) of all atoms being only c.a. 0.13 Å. The B atoms in the $B_8$ island and the adsorbed H atoms do move during the simulation, with a relatively large RMSD of c.a. 0.30 Å and c.a. 0.37 Å, respectively, but there is no bond breakage, nor H migration. In conclusion, despite the weakening of the conjugated system over the $B_8$ island, the surface should maintain its structural integrity at room temperature.

To quantitatively study the electron transfer accompanying the adsorption events on the $B_8$ island, we calculate the Bader charge of the atoms in 1H#1, 2H#1, 2H#2, 3H#1, 4H#1, and 5H#1, as summarized in Figure S4. The H gains a ∼0.4 negative charge upon adsorption as a result of the electron transfer from the top-layer B in 1H#1, suggesting that a more negative Bader charge on the site would facilitate adsorption. The other B atoms in the $B_8$ island also gain a negative charge of −0.02 to −0.12 due to the disruption of the conjugated system, activating them to be more favorable adsorption sites under higher coverages. The H adsorption on type-1 W, however, does not lead to a so pronounced charge transfer to the surrounding atoms. As we increase the H coverage from 1 to 4 and focus on surface states where top-layer Bs act as adsorption sites, the sum of the Bader charges of top-layer Bs keeps increasing, while sub-layer Bs gain a share of electrons released from disruption of the conjugate system (Figure 3c). Overall, the $B_8$ island loses electrons with an increasing H coverage. In Figure 3b, it can be seen that the charge transfer to H is mostly contributed by the $B_8$ island with little participation of the WB substrate, indicating that the restructured layer of excess boron could be generally present on borides and the intrinsic properties of the B-rich layer is somewhat substrate-independent. This qualitative conclusion also likely translates to the (111) surface of WB, which we did not investigate here.

After understanding the change in the electronic structure induced by the adsorption of adsorbates, we go back to investigate the HER activity. The hydrogen evolution reaction has two steps

$$* + H^+ + e^- \rightarrow *H \quad (1)$$

$$*H + H^+ + e^- \rightarrow * + H_2 \quad (2)$$

where the * and *H stand for the active site and the adsorbed H species on the surface, respectively. The chemical potential of $H^+$ and $e^-$ can be expressed by the chemical potential of hydrogen gas using the computational hydrogen electrode model. Since the activation barrier of the proton−electron transfer has been demonstrated by numerical calculations and theoretical considerations to scale with $\Delta G$,[27−29] the barrier of HER steps can be described by $\Delta G_H$.[30] It comes naturally that the optimal HER active site would have $|\Delta G_H| \approx 0$ because too positive $\Delta G_H$ means difficulty in step (1), while too negative $\Delta G_H$ leads to a slow step (2). Note that the possibility of the Volmer−Tafel mechanism is also tested, but the energy barrier for dihydrogen formation from two *H is too high (>1.5 eV), and the Volmer−Heyrovsky mechanism prevails. This is probably due to the more directional H binding and less favorable H migration on the $B_8$ unit as compared to the case on noble metals such as Pt.

In conventional practice, the most stable structure, or the GM, at each coverage would be used to calculate the $|\Delta G_H|$, which would then serve as the activity descriptor for the HER. However, the structural diversity of our $B_8$ island surface under different coverages casts doubt on the conventional practice: although 1H#1 is more stable than 1H#2, it structurally mismatches 2H#1 (Figure 3), the most stable surface state


https://dx.doi.org/10.1021/acscatal.0c03410
ACS Catal. XXXX, XXX, XXX−XXX

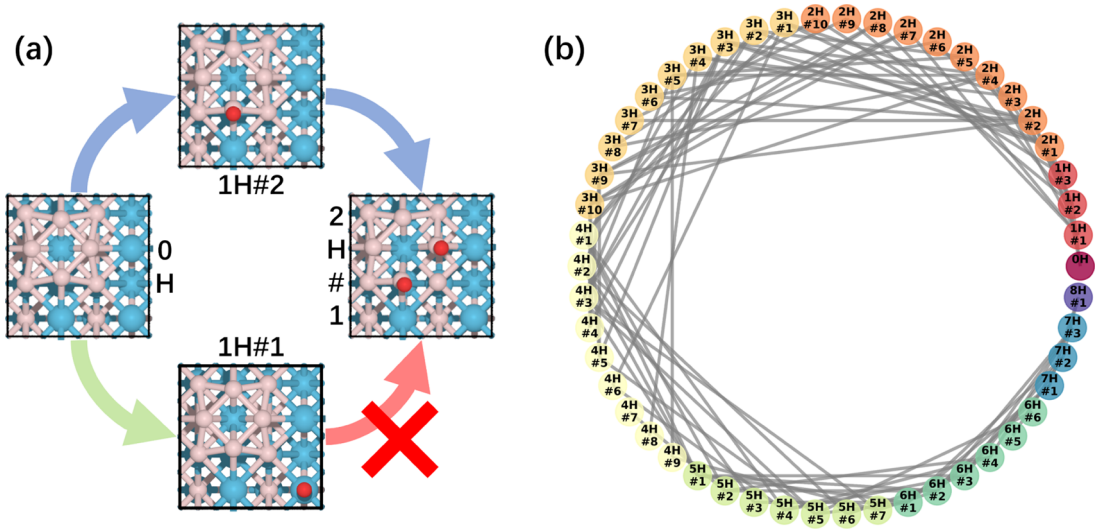


**Figure 4.** (a) Illustration of accepted and rejected HER reaction paths connecting minima. Color code: H (red), B (pink), and W (blue). (b) Full reaction map of all viable reaction pathways based on the found minima in this study. Each node in the graph represents a surface state with its color showing its corresponding adsorbate coverage (warmer: lower coverage and colder: higher coverage). Every connecting line stands for a reaction path with a matched geometry between the initial and final states.

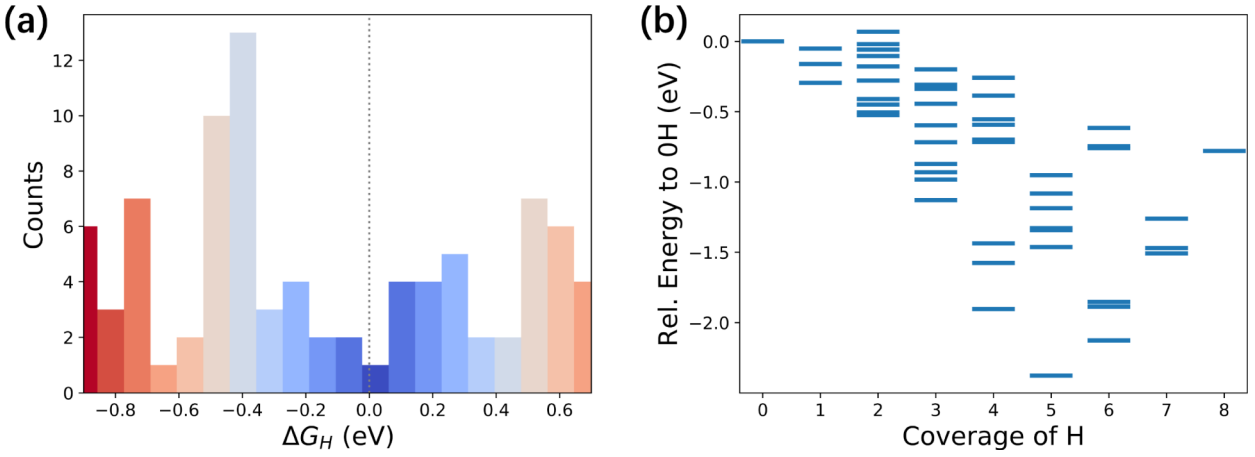


**Figure 5.** (a) Histograms showing the distribution of $\Delta G_H$ of the feasible HER pathways, with the cold and warm colors representing favorable and unfavorable HER energetics, respectively. The dashed line marks the optimal $\Delta G_H$ value for HER. (b) Relative free energies of each surface state from different coverages under the grand canonical scheme at $U$ = 0 V (vs SHE) and $p$H = 0, with the 0H surface state as the zero reference.

under a 2H coverage; instead, it is the thermally accessible 1H#2 and 1H#3 metastable states that can uptake an additional H to become 2H#1. In terms of geometry, only if the * and *H intermediates structurally match will the reaction step make chemical sense. The infeasibility is supported by energetics: going from 1H#2 to 2H#1 only involves a single step H-adsorption, while going from 1H#1 to 2H#1 requires a direct migration of adsorbed H from type-1 W to top-layer B beforehand, which is not only thermodynamically uphill but also has a prohibitively high barrier of 1.67 eV (Figure S5). Therefore, some reaction paths with seemingly favorable energetics should be excluded if the geometries of the initial and final species do not match. Hence, we include all of the local minima at each coverage into our model, and evaluate the structural similarity of each possible pairs of * and *H. To be specific, we calculated the mean atomic displacement ($D$) for each pair of * and *H

$$D = \frac{1}{N}\sum_{n=1}^{N} |\boldsymbol{r}_{n,\mathrm{f}} - \boldsymbol{r}_{n,\mathrm{i}}|$$

Here $N$ is the total number of atoms in *, $\boldsymbol{r}_n$ is the position vector of the $n$th atom in the structure, and i and f stand for the initial and final states, respectively. By eliminating the */*H pairs with a mean atomic displacement larger than 0.025 Å, we keep only 88 relevant pairs (listed in Supporting Note 1) out of the 349 pairs and plot them into a circular graph in Figure 4. The nodes represent surface states, and they are colored in a spectral color map according to the H coverage. Each edge connecting a */*H pair represents a unique HER catalytic cycle, interweaving into a complex reaction network.

Figure 5a shows the distribution of $\Delta G_H$ of all of the feasible HER pathways in Figure 4b with the region near $\Delta G_H$ = 0 marked by a gray dotted line. It is a rather wide distribution ranging from c.a. −0.9 to +0.7 eV, indicating binding sites of diverse electronic structures that result from different adsorbate coverages and configurations. There are some


https://dx.doi.org/10.1021/acscatal.0c03410
ACS Catal. XXXX, XXX, XXX−XXX

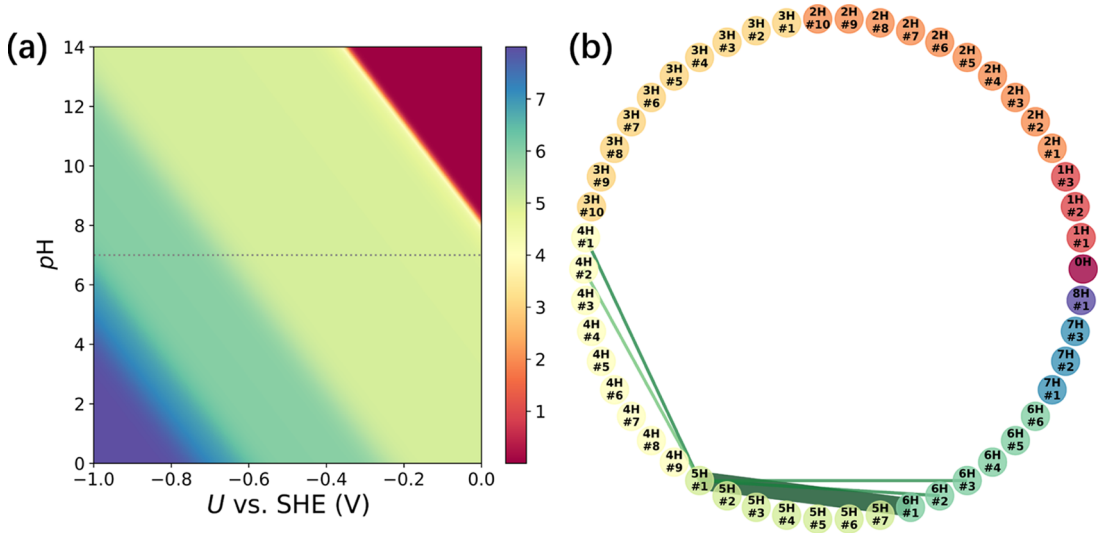


**Figure 6.** (a) Phase diagram of the hydrogen coverage on the $B_8$-decorated surface as a function of *p*H and the applied potential. The gray dotted lines mark the neutral pH condition. (b) Revised reaction map that also shows the activity contribution from each reaction pathway, with the major contributor in the thicker line and darker green while minor contributors in the thinner line and lighter green.

pathways with optimum $\Delta G_H$, however, we may have very few of them in the reaction conditions to contribute significantly to the overall activity. Hence, it is crucial to quantitatively calculate the population of each surface state. In a realistic scenario, the surface exists as an ensemble of surface states of different adsorption configurations within each coverage, and every surface state contributes to the overall activity to some extent.[31] To obtain the population of each surface state, a grand canonical ensemble can be established based on the grand canonical free energy Ω

$$\Omega = A(^*nH) - n\mu_{H^+}(U, pH) - n\mu_{e^-}(U, pH)$$

where $n$ is the number of adsorbed H atoms and $A(^*nH)$ is the free energy of the surface state with n adsorbed H atoms. $\mu_{H^+}(U, pH)$ and $\mu_{e-}(U, pH)$ are the electrochemical potentials of protons and electrons. Under the CHE scheme, the chemical potential of an electron−proton pair can be approximated in reference to the free energy of half a dihydrogen molecule, and it also allows the effect of the applied potential and *p*H to be easily included in the model.[32,33] Figure 5b shows the free energies of the surface states of different H coverages relative to the 0H case at $U = 0$ V (vs SHE) and *p*H = 0. The 5H#1 has the lowest energy among all surface states and is therefore the most populated state at that specific reaction condition. Since changes in $U$ and *p*H can reshape the energy landscape by altering the $\mu_H$ term, the global minimum of the grand canonical ensemble can shift under different reaction conditions. Since the aqueous solution can act as a proton reservoir at a finite temperature and protons can diffuse through the water−hydronium network without much of a kinetic barrier, we assume the ensemble to be ergodic, i.e., surface states with the same or different coverage can interconvert and reach an equilibrium. Therefore, the population of each surface state can be calculated by the Boltzmann distribution

$$p_i = \frac{\exp(-\frac{\Omega_i}{kT})}{\sum_{j=1}^{N}\exp\left(-\frac{\Omega_j}{kT}\right)}$$

where in this case $T = 298$ K. The population of each surface state can then be readily calculated under any given reaction conditions. In Figure 6a, the ensemble-averaged H coverage is shown as a function of $U$ and *p*H in their experimental range. In alkaline media, the $B_8$ unit remains structurally intact and the surface tends to stay intact in the 0H coverage. When the $\mu_H$ increases to a threshold by increasing acidity or applying more negative potential, the surface quickly converts to the 4H coverage over a very small range of $\mu_H$. This can be attributed to the activation of neighboring B sites in the $B_8$ unit upon the first H adsorption until all four top-layer B atoms are covered, which is discussed in previous sections. After that, the 4H surface states accept another H onto the type-1 W site and stay in the 5H coverage over a quite wide window of $\mu_H$. Note that in the realistic scenario of HER in alkaline media, an alternative reaction mechanism with different kinetics may come into play, therefore the reactivity evaluation based on the grand canonical ensemble would only hold in the neutral−acidic media. Since the HER is usually performed with a pH ranging from 0 to 7 and $U$ ranging from 0 to −0.5 V vs SHE, we would expect only the 5H and higher coverages in the working conditions.

It is then clear that neither the population nor $|\Delta G_H|$ can act as a proper descriptor of the HER activity, and both must be included in our model. Since $\Delta G$ of an electrochemical step under CHE scheme scales with the electrochemical barrier, the reaction rate of the elementary redox steps (1) and (2) involving any feasible pair of * and *H (denoted as $i$ and $j$) under a constant pH can be expressed by the Arrhenius-type equation as

$$\text{step 1:} \quad r_{f,ij} = k_{f,ij}[^*] \propto \exp\left(-\frac{\Delta G_f(U)}{kT}\right)\cdot p_i$$

$$\text{step 2:} \quad r_{r,ij} = k_{r,ij}[^*H] \propto \exp\left(-\frac{\Delta G_r(U)}{kT}\right)\cdot p_j$$

where $\Delta G_f(U)$ and $\Delta G_r(U)$ are the potential-dependent free energy change of the forward (1) and reverse (2) reaction steps, and $p_i$ and $p_j$ are the population of the * and *H sites calculated from the Boltzmann distribution in the grand


https://dx.doi.org/10.1021/acscatal.0c03410
ACS Catal. XXXX, XXX, XXX−XXX

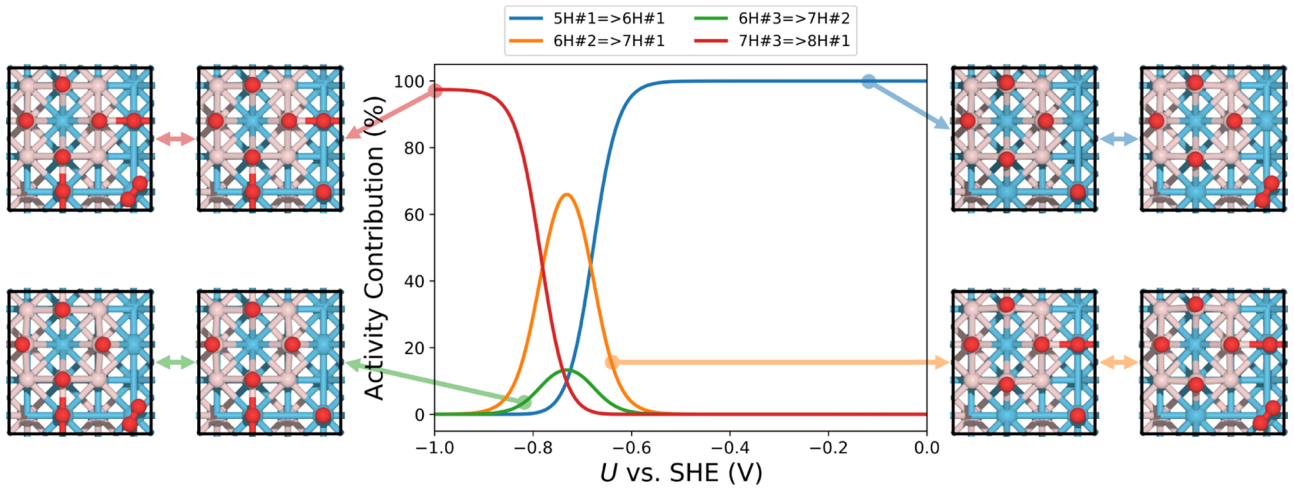


**Figure 7.** Activity contribution in percentages of the four most active surface states versus applied potential. The optimized geometries of the involved surface states are shown on the left and right sides of the plot. Color code: H (red), B (pink), and W (blue).

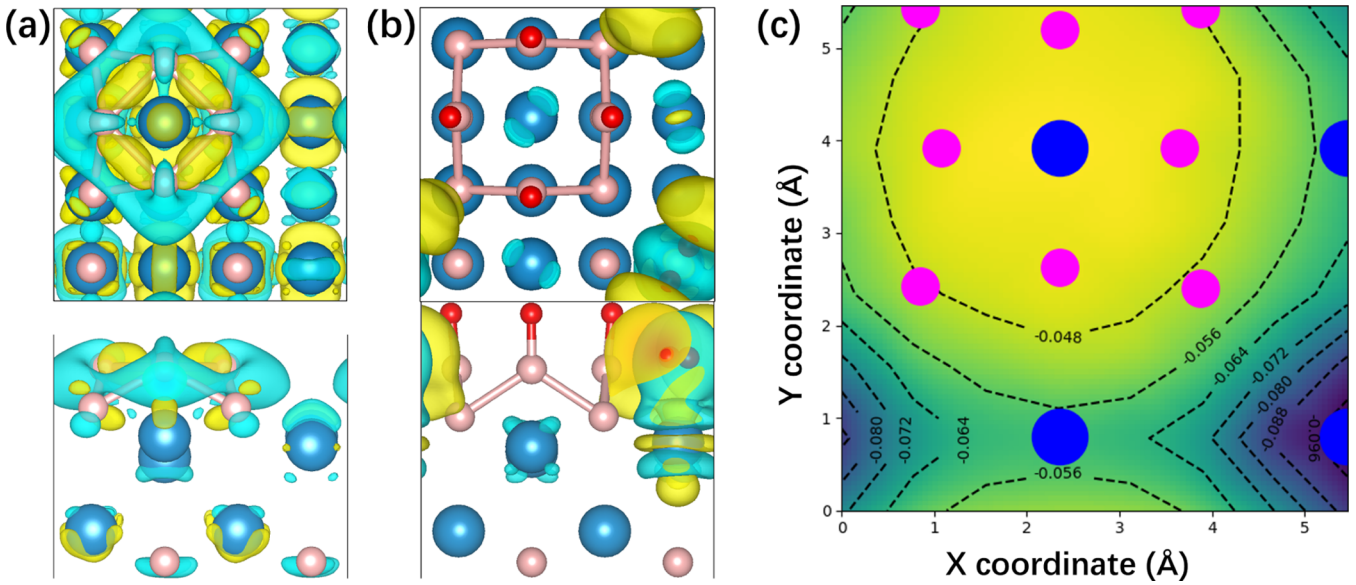


**Figure 8.** Electron density difference map of (a) $B_8$ unit interacting with the WB substrate and (b) dihydrogen-mode adsorption on type-I W in the 6H global minimum configuration at an isovalue = 0.0015, with blue and yellow isosurfaces representing the increase and decrease in the electron density, respectively. (c) Potential energy surface of $H_2$ adsorbed on the $B_8$-decorated surface with value-labeled contours (in eV), with warm and cold colors representing unfavorable and favorable physisorption energies, respectively. Color code: H (red), B (pink), and W (blue).

canonical ensemble, respectively. The overall rate $r_{ij}$ of the step concerning surface states $i$ and $j$ can then be calculated from a Butler–Volmer-type equation

$$r_{ij} \propto \exp\left(-\alpha\frac{\Delta G_f(U)}{kT}\right)\cdot p_i - \exp\left(-(1-\alpha)\frac{\Delta G_r(U)}{kT}\right)\cdot p_j$$

where $\alpha \in [0,1]$ is the mechanistic symmetry factor. Here, we adopt the value of $\alpha = 0.5$ assuming no asymmetry about the equilibrium potential. The net rate $r_{net}$ of the HER involving $i$ and $j$ is taken to be the smaller overall rate between those of steps (1) and (2), and it could act as a descriptor of the activity contribution from a specific pathway. In Figure 5b, we replot the edges representing the */*H reaction pairs with a color map and thicken the edges with aPotential energy surface large $r_{ij}$ (evaluated at $p$H = 0 and $U$ = 0.1 V vs SHE). The */*H pairs with the largest HER rates are 5H#1/6H#1, 4H#1/5H#1, 5H#1/6H#2, and 5H#1/6H#3. Although the 5H#1/6H#1 pathway does not have fully optimal $|\Delta G_H|$, the 5H#1 surface state has so dominant population that the 5H#1-related pathways prevail in terms of the net HER rate. Some other pathways with a near-zero $|\Delta G_H|$, such as 2H#1/3H#3 and 2H#6/3H#6, turn out to show negligible activity since the related surface states are inaccessible. The weighted reaction map presents a vivid illustration that it is the surface states with significant population and decent energetics, instead of the ones with the most optimal $|\Delta G_H|$, that contribute to the overall reactivity.

It is also straightforward to track the effect of varying overpotentials on site contributions to the overall HER rate based on this grand canonical ensemble representation. In Figure 7, we break down the total HER rates to percentage contributions of the four major pathways at $p$H = 0. In the potential range of 0 to −0.5 V vs SHE, the HER is solely contributed by the 5H#1/6H#1 pathway. The 5H#1/6H#1 has a $|\Delta G_H|$ of 0.249 eV, corresponding to an overpotential of


https://dx.doi.org/10.1021/acscatal.0c03410
ACS Catal. XXXX, XXX, XXX−XXX

249 mV, which is in good agreement with the experimental value on tungsten boride in the $U$ = 0 to −0.5 V range (given value).[10] As the potential goes to −0.6 V vs SHE, the 6H surface states gain population, and 5H loses, so that the 6H#2/7H#1 and 6H#3/7H#2 become the top two contributors to the overall HER activity, which correspond to an overpotential of ∼380 mV if not limited by population. At more negative potentials, the 8H coverage, also the completely hydrogenated form, gets populated, and the 7H#3/8H#1 becomes the major reaction pathway with an overpotential of 480 mV, if not limited by the population. It is seen that, as the potential gets more negative, the surface is driven into a higher H coverage region where the accessible HER pathways involve low-population metastable sites and have inferior intrinsic reactivity compared to the lower-coverage cases. This suggests a reactivity decline of the boride catalysts at high overpotentials or in too acidic media. Such a trend is similar to the HER on metal surfaces where reactivity of the surface is optimal under an intermediate H coverage but worsens near the full coverage. Note that many of the surface states involved are accessible local minima of their coverage, and they are necessary for a full and correct depiction of the HER process on $B_8$-decorated WB (001).

It is somewhat surprising that all of the major contributing pathways involve the same W−H/W−$H_2$ cycle on the type-1 W site, motivating us to further investigate the role of the $B_8$ island at higher coverage cases. The electron density difference map in Figure 8a shows that, upon the formation of the $B_8$ island on the surface, the electron density on the type-2 W is depleted, while the density on the type-1 W increases. In addition, the electron density from the $B_8$ unit spreads out to cover the region over type-2 W sites, destabilizing the W−H configuration, and the formation of W−$H_2$ on the type-2 W sites. Figure 8b shows the bonding nature of the W−$H_2$ unit: a small amount of electron is donated by type-1 W to the region between the two H atoms above (also evidenced by the Bader charge in Figure S4), forming W−H bonds while also giving rise to a $\sigma$-type bond between two H adsorbates. However, the change in the electron density over type-1 W induced by the formation of $B_8$ is actually minor, and the energetics of the W−H/W−$H_2$ cycle is similar to the $B_8$-decorated and the bare WB (001). The major role of $B_8$ is that it suppresses H adsorption on type-2 W sites next to the active type-1 W site, and ensures that the surface state with the W−$H_2$ unit has a significant population at higher H coverages. Such suppression is absent on the stoichiometric WB (001) surface where the second H adsorbate tends to reside on the neighboring W site instead of forming a favorable W−$H_2$ species (Figure S2). In addition, the physisorption of $H_2$ on the $B_8$ unit is unfavorable (Figure 8c), and such effect extends to the region over the type-2 W sites, effectively isolating the active type-1 W atoms from each other in a single-site fashion. This should have an unusual and important effect on the HER activity of the B-rich surface: The formed $H_2$ will not accumulate as large flat gas bubbles cover the surface of catalysts and passivate it. The bubble effect is a common problem in HER on catalysts where active sites are densely distributed, such as metals, phosphides, and chalcogenides.[34] The $B_8$ islands that were formed from restructuring of excess boron could effectively act as sub-nano aerophobic units and prevent the gas accumulation problem. This could also explain the outstanding stability of the borides in long-term and high-current-density electrocatalysis without elaborate nanostructuring.[10]

## CONCLUSIONS

In summary, we applied global optimization combined with DFT to explore the surface restructuring of WB (001) and the diverse adsorption configurations under different adsorbate coverages. Based on the obtained surface states from global optimization, we constructed a reaction network by checking the geometric similarity of the surface states of different coverages. A grand canonical ensemble is proposed based on the found minima to establish a phase diagram of adsorbate coverages as a function of $p$H and the applied potential. The contribution to the overall activity by each surface state is calculated to reveal an intricate reaction network involving the coexisting surface states of different adsorbate coverages and configurations. The ensemble-averaged reaction rate suggests that the HER activity heavily depends on a few states featuring the W−H/W−$H_2$ catalytic cycle, which emerge only at higher coverages on a reconstructed surface. The population of metastable states may be further tuned by altering the adsorbate coverage (solute concentration, $p$H), window of the applied potential, temperature, controlling the over-stoichiometric amount of boron on the surface, or adding dopants to optimize the performance of the catalyst. In addition, the $B_8$ island is demonstrated to be $H_2$-phobic and could isolate the active W sites from each other to prevent passivation of the catalysts due to $H_2$ bubble accumulation. Given that boron-rich interfaces are likely typical for most metal borides,[19,21] this passivation-prevention mechanism could be a general feature of HER-active borides. The study emphasizes the necessity to include surface restructuring and varying adsorbate configurations when looking for the active sites, instead of focusing on the (putative) global minimum or a static bare surface. Resorting to the ensemble representation, despite the cost, has been proven rewarding given the rich chemistry it unlocked and a more realistic picture of the catalysis we can capture.

## COMPUTATIONAL METHODS

The bare WB (001) is modeled by a 2 × 2 × 7 supercell with the upper three layers relaxed as the surface region and lower four layers constrained as the bulk region. A vacuum slab of 15 Å thickness is added in the $Z$ direction to avoid spurious interactions between periodic images.

Global optimizations for the surface terminations in B-rich conditions are performed using the particle-swarm optimization (PSO),[35] which is an efficient evolutionary algorithm for sampling of ground-state and metastable structures in complex solid or surface systems. PSO performs this sampling (search for the most stable structures) by having a population of candidate geometries, which move in the search space, under the influence of their own positions and velocities, and are also guided by other geometries toward the constantly updated and currently best one. This moves the swarm toward the best solutions. The simulation is performed using CALYPSO software,[36] following the procedure explained in a previous study.[23] The adsorbate configurations of H on B-rich surfaces under different coverages are exhaustively sampled by screening through all possible combinations due to a relatively small chemical space. The generated structures are optimized with the revised Perdew−Burke−Ernzerhof (RPBE) functional[37] and projector augmented wave (PAW) pseudopotentials[38] using the Vienna Ab initio Simulation Package (VASP) program.[39−42] D3 correction is used to account for the


https://dx.doi.org/10.1021/acscatal.0c03410
ACS Catal. XXXX, XXX, XXX−XXX

dispersion interactions,[43] and dipole corrections are applied to remove the artificial electrostatic fields arising from asymmetric slabs in periodic boundary conditions. The convergence criteria for the geometry (SCF) was set to $10^{-5}$ ($10^{-6}$) eV and $10^{-2}$ eV/Å for forces. A 4 × 4 × 1 Γ-centered *k*-point grid was used and the cutoff energy for the kinetic energy of the plane-waves was 450 eV. Note that although a canonical DFT scheme instead of a grand canonical DFT one is employed here, the Fermi level shift upon adding the adsorbate was calculated to be ∼0.05 eV, hence the results obtained should only deviate minorly from the grand canonical DFT treatments.

The surface energies were calculated as

$$\gamma = \frac{1}{2A}\left(E_{\text{slab}} - \sum N_X \mu_X\right)$$

where $A$ is the area of the supercell, $E_{\text{slab}}$ is the energy of the surface slab, $N_X$ is the number of $X$ atoms in the slab, and $\mu_X$ is the chemical potential of the $X$ atom. The chemical potential of W and B are calculated from bulk WB for the stoichiometric part, while from bulk FCC W and bulk elemental B for the nonstoichiometric part, respectively. The surface energy of asymmetric slabs are calculated by canceling out the contribution using a corresponding symmetric slab following the protocol explained in ref 44.

The adsorption energy is calculated by

$$\Delta E_{\text{H}} = E(^*\text{H}) - E(^*) - E(\text{H})$$

where the * stands for the adsorption site. The adsorption free energy of H is calculated by

$$\Delta G_{\text{H}} = \Delta E_{\text{H}^*} + \text{ZPE} - T\Delta S_{\text{H}}$$

where the latter two terms (ZPE and entropy term at room temperature) are taken from the literature to be +0.24 eV.[27]

In the grand canonical ensemble, the population of each surface state is calculated by the Boltzmann distribution based on the grand canonical free energy. The chemical potential of $H^+$ and $e^-$ can be expressed using the computational hydrogen electrode model[27]

$$\mu_{\text{H}}(U, \text{pH}) = \frac{1}{2}\mu(\text{H}_2) - eU + k_{\text{B}}T\text{pH}$$

where $\mu(H_2)$ is the chemical potential of the hydrogen molecule in the gas state and $U$ is referenced against the standard hydrogen electrode (SHE).

The transition states (TS) are obtained using the climbing image nudged elastic band (CI-NEB) method[45] and each TS geometry has been calculated to have only one imaginary mode. The Bader charges are calculated from the VASP output using the Bader Charge Analysis code.[46]

Molecular dynamics (MD) simulations are performed using VASP. The NVT ensemble simulation is performed at 500 K for 5 ps duration with a time step of 1 fs. A Nosé−Hoover thermostat was used, and the image was collected every 50 fs after the system was considered to be equilibrated.

## ■ ASSOCIATED CONTENT

### Supporting Information

The Supporting Information is available free of charge at https://pubs.acs.org/doi/10.1021/acscatal.0c03410.

Surface energy of explored surface terminations; binding energy of adsorbates; geometry and relative energy of low-energy minima at 1H−8H coverages; transition states of H migration on $B_8$; RMSD of H-coveraged $B_8$ during BOMD; calculated Bader charges; and a list of chemically relevant reaction pairs (PDF)

## ■ AUTHOR INFORMATION


### Corresponding Author

**Anastassia N. Alexandrova** − *Department of Chemistry and Biochemistry and Department of Chemical and Biomolecular Engineering, University of California, Los Angeles, Los Angeles, California 90095, United States;* orcid.org/0000-0002-3003-1911; Email: ana@chem.ucla.edu

### Authors

**Zisheng Zhang** − *Department of Chemistry and Biochemistry, University of California, Los Angeles, Los Angeles, California 90095, United States*

**Zhi-Hao Cui** − *Department of Chemistry and Biochemistry, University of California, Los Angeles, Los Angeles, California 90095, United States;* orcid.org/0000-0002-7389-4063

**Elisa Jimenez-Izal** − *Kimika Fakultatea, Euskal Herriko Unibertsitatea (UPV/EHU) and Donostia International Physics Center (DIPC), 20080 Donostia, Euskadi, Spain; IKERBASQUE, Basque Foundation for Science, 48009 Bilbao, Euskadi, Spain*

**Philippe Sautet** − *Department of Chemistry and Biochemistry, Department of Chemical and Biomolecular Engineering, and California NanoSystems Institute, University of California, Los Angeles, Los Angeles, California 90095, United States;* orcid.org/0000-0002-8444-3348

Complete contact information is available at: https://pubs.acs.org/10.1021/acscatal.0c03410


### Notes

The authors declare no competing financial interest.

## ■ ACKNOWLEDGMENTS

This work was funded by the DOE-BES Grant DE-SC0019152. This research used resources of the National Energy Research Scientific Computing Center (NERSC), a U.S. Department of Energy Office of Science User Facility operated under Contract No. DE-AC02-05CH11231. An award of the computer time was provided by the Innovative and Novel Computational Impact on Theory and Experiment (INCITE) program. This research used resources of the Argonne Leadership Computing Facility, which is a DOE Office of Science User Facilities supported under Contract DE-AC02-06CH11357.

## ■ REFERENCES

(1) Yan, Y.; Xia, B. Y.; Zhao, B.; Wang, X. A Review on Noble-Metal-Free Bifunctional Heterogeneous Catalysts for Overall Electrochemical Water Splitting. *J. Mater. Chem. A* **2016**, *4*, 17587−17603.

(2) Anantharaj, S.; Ede, S. R.; Sakthikumar, K.; Karthick, K.; Mishra, S.; Kundu, S. Recent Trends and Perspectives in Electrochemical Water Splitting with an Emphasis on Sulfide, Selenide, and Phosphide Catalysts of Fe, Co, and Ni: A Review. *ACS Catal.* **2016**, *6*, 8069−8097.

(3) Carenco, S.; Portehault, D.; Boissière, C.; Mézailles, N.; Sanchez, C. Nanoscaled Metal Borides and Phosphides: Recent Developments and Perspectives. *Chem. Rev.* **2013**, *113*, 7981−8065.

(4) Alexandrova, A. N.; Boldyrev, A. I.; Zhai, H.-J.; Wang, L.-S. All-Boron Aromatic Clusters as Potential New Inorganic Ligands and



https://dx.doi.org/10.1021/acscatal.0c03410
ACS Catal. XXXX, XXX, XXX−XXX

Building Blocks in Chemistry. *Coord. Chem. Rev.* **2006**, *250*, 2811−2866.
(5) Scheifers, J. P.; Zhang, Y.; Fokwa, B. P. T. Boron: Enabling Exciting Metal-Rich Structures and Magnetic Properties. *Acc. Chem. Res.* **2017**, *50*, 2317−2325.
(6) Gupta, S.; Patel, N.; Miotello, A.; Kothari, D. C. Cobalt-Boride: An Efficient and Robust Electrocatalyst for Hydrogen Evolution Reaction. *J. Power Sources* **2015**, *279*, 620−625.
(7) Borodzínski, J. J.; Lasia, A. Electrocatalytic Properties of Doped Nickel Boride Based Electrodes for the Hydrogen Evolution Reaction. *J. Appl. Electrochem.* **1994**, *24*, 1267−1275.
(8) Jothi, P. R.; Zhang, Y.; Scheifers, J. P.; Park, H.; Fokwa, B. P. T. Molybdenum Diboride Nanoparticles as a Highly Efficient Electrocatalyst for the Hydrogen Evolution Reaction. *Sustainable Energy Fuels* **2017**, *1*, 1928−1934.
(9) Jothi, P. R.; Zhang, Y.; Yubuta, K.; Culver, D. B.; Conley, M.; Fokwa, B. P. T. Abundant Vanadium Diboride with Graphene-like Boron Layers for Hydrogen Evolution. *ACS Appl. Energy Mater.* **2019**, *2*, 176−181.
(10) Park, H.; Zhang, Y.; Lee, E.; Shankhari, P.; Fokwa, B. P. T. High-Current-Density HER Electrocatalysts: Graphene-like Boron Layer and Tungsten as Key Ingredients in Metal Diborides. *ChemSusChem* **2019**, *12*, 3726−3731.
(11) Robinson, P. J.; Liu, G.; Ciborowski, S.; Martinez-Martinez, C.; Chamorro, J. R.; Zhang, X.; McQueen, T. M.; Bowen, K. H.; Alexandrova, A. N. Mystery of Three Borides: Differential Metal−Boron Bonding Governing Superhard Structures. *Chem. Mater.* **2017**, *29*, 9892−9896.
(12) Li, Q.; Zhou, D.; Zheng, W.; Ma, Y.; Chen, C. Anomalous Stress Response of Ultrahard WB n Compounds. *Phys. Rev. Lett.* **2015**, *115*, No. 185502.
(13) Itoh, H.; Matsudaira, T.; Naka, S.; Hamamoto, H.; Obayashi, M. Formation Process of Tungsten Borides by Solid State Reaction between Tungsten and Amorphous Boron. *J. Mater. Sci.* **1987**, *22*, 2811−2815.
(14) Matsudaira, T.; Itoh, H.; Naka, S.; Hamamoto, H.; Obayashi, M. Synthesis and Reaction Sintering of WB. *Int. J. High Technol. Ceram.* **1987**, *3*, 337−338.
(15) Yeung, M. T.; Mohammadi, R.; Kaner, R. B. Ultra-incompressible, Superhard Materials. *Annu. Rev. Mater. Res.* **2016**, *46*, 465−485.
(16) Fan, C.; Liu, C.; Peng, F.; Tan, N.; Tang, M.; Zhang, Q.; Wang, Q.; Li, F.; Wang, J.; Chen, Y.; et al. Phase Stability and Incompressibility of Tungsten Boride (WB) Researched by in-Situ High Pressure X-Ray Diffraction. *Phys. B: Condens. Matter* **2017**, *521*, 6−12.
(17) Dong, H.; Dorfman, S. M.; Chen, Y.; Wang, H.; Wang, J.; Qin, J.; He, D.; Duffy, T. S. Compressibility and Strength of Nanocrystalline Tungsten Boride under Compression to 60 GPa. *J. Appl. Phys.* **2012**, *111*, No. 123514.
(18) Kayhan, M.; Hildebrandt, E.; Frotscher, M.; Senyshyn, A.; Hofmann, K.; Alff, L.; Albert, B. Neutron Diffraction and Observation of Superconductivity for Tungsten Borides, WB and W2B4. *Solid State Sci.* **2012**, *14*, 1656−1659.
(19) Grant, J. T.; McDermott, W. P.; Venegas, J. M.; Burt, S. P.; Micka, J.; Phivilay, S. P.; Carrero, C. A.; Hermans, I. Boron and Boron-Containing Catalysts for the Oxidative Dehydrogenation of Propane. *ChemCatChem* **2017**, *9*, 3623−3626.
(20) Grant, J. T.; Carrero, C. A.; Goeltl, F.; Venegas, J.; Mueller, P.; Burt, S. P.; Specht, S. E.; McDermott, W. P.; Chieregato, A.; Hermans, I. Selective Oxidative Dehydrogenation of Propane to Propene Using Boron Nitride Catalysts. *Science* **2016**, *354*, 1570−1573.
(21) Zhang, Z.; Jimenez-Izal, E.; Hermans, I.; Alexandrova, A. N. Dynamic Phase Diagram of Catalytic Surface of Hexagonal Boron Nitride under Conditions of Oxidative Dehydrogenation of Propane. *J. Phys. Chem. Lett.* **2019**, *10*, 20−25.
(22) Venegas, J. M.; Zhang, Z.; Agbi, T. O.; McDermott, W. P.; Alexandrova, A.; Hermans, I. Why Boron Nitride Is Such a Selective Catalyst for the Oxidative Dehydrogenation of Propane. *Angew. Chem., Int. Ed.* **2020**, *59*, 16527−16535.
(23) Cui, Z.-H.; Jimenez-Izal, E.; Alexandrova, A. N. Prediction of Two-Dimensional Phase of Boron with Anisotropic Electric Conductivity. *J. Phys. Chem. Lett.* **2017**, *8*, 1224−1228.
(24) De La Pierre, M.; Bruno, M.; Manfredotti, C.; Nestola, F.; Prencipe, M.; Manfredotti, C. The (100), (111) and (110) Surfaces of Diamond: An Ab Initio B3LYP Study. *Mol. Phys.* **2014**, *112*, 1030−1039.
(25) Li, X.; Wang, Y. X.; Lo, V. C. First-Principles Study of the (001) and (110) Surfaces of Superhard $ReB_2$. *Thin Solid Films* **2012**, *520*, 4951−4955.
(26) Silvi, B.; Savin, A. Classification of Chemical Bonds Based on Topological Analysis of Electron Localization Functions. *Nature* **1994**, *371*, 683−686.
(27) Nørskov, J. K.; Bligaard, T.; Logadottir, A.; Kitchin, J. R.; Chen, J. G.; Pandelov, S.; Stimming, U. Trends in the Exchange Current for Hydrogen Evolution. *J. Electrochem. Soc.* **2005**, *152*, J23−J26.
(28) Lindgren, P.; Kastlunger, G.; Peterson, A. A. A Challenge to the G ∼ 0 Interpretation of Hydrogen Evolution. *ACS Catal.* **2020**, *10*, 121−128.
(29) Melander, M. M. Grand Canonical Rate Theory for Electrochemical and Electrocatalytic Systems I: General Formulation and Proton-Coupled Electron Transfer Reactions. *J. Electrochem. Soc.* **2020**, *167*, No. 116518.
(30) Bligaard, T.; Nørskov, J. K.; Dahl, S.; Matthiesen, J.; Christensen, C. H.; Sehested, J. The Brønsted−Evans−Polanyi Relation and the Volcano Curve in Heterogeneous Catalysis. *J. Catal.* **2004**, *224*, 206−217.
(31) Zhang, Z.; Zandkarimi, B.; Alexandrova, A. N. Ensembles of Metastable States Govern Heterogeneous Catalysis on Dynamic Interfaces. *Acc. Chem. Res.* **2020**, *53*, 447−458.
(32) Karmodak, N.; Andreussi, O. Catalytic Activity and Stability of Two-Dimensional Materials for the Hydrogen Evolution Reaction. *ACS Energy Lett.* **2020**, *5*, 885−891.
(33) Hörmann, N. G.; Andreussi, O.; Marzari, N. Grand Canonical Simulations of Electrochemical Interfaces in Implicit Solvation Models. *J. Chem. Phys.* **2019**, *150*, No. 041730.
(34) Lu, Z.; Zhu, W.; Yu, X.; Zhang, H.; Li, Y.; Sun, X.; Wang, X.; Wang, H.; Wang, J.; Luo, J.; et al. Ultrahigh Hydrogen Evolution Performance of Under-Water "Superaerophobic" $MoS_2$ Nanostructured Electrodes. *Adv. Mater.* **2014**, *26*, 2683−2687.
(35) Wang, Y.; Lv, J.; Zhu, L.; Ma, Y. Crystal Structure Prediction via Particle-Swarm Optimization. *Phys. Rev. B* **2010**, *82*, No. 094116.
(36) Wang, Y.; Lv, J.; Zhu, L.; Ma, Y. CALYPSO: A Method for Crystal Structure Prediction. *Comput. Phys. Commun.* **2012**, *183*, 2063−2070.
(37) Hammer, B.; Hansen, L. B.; Nørskov, J. K. Improved Adsorption Energetics within Density-Functional Theory Using Revised Perdew-Burke-Ernzerhof Functionals. *Phys. Rev. B* **1999**, *59*, No. 7413.
(38) Kresse, G.; Joubert, D. From Ultrasoft Pseudopotentials to the Projector Augmented-Wave Method. *Phys. Rev. B* **1999**, *59*, No. 1758.
(39) Kresse, G.; Furthmüller, J. Efficiency of Ab-Initio Total Energy Calculations for Metals and Semiconductors Using a Plane-Wave Basis Set. *Comput. Mater. Sci.* **1996**, *6*, 15−50.
(40) Kresse, G.; Furthmüller, J. Efficient Iterative Schemes for Ab Initio Total-Energy Calculations Using a Plane-Wave Basis Set. *Phys. Rev. B* **1996**, *54*, No. 11169.
(41) Kresse, G.; Hafner, J. Ab Initio Molecular Dynamics for Liquid Metals. *Phys. Rev. B* **1993**, *47*, No. 558.
(42) Kresse, G.; Hafner, J. Ab Initio Molecular-Dynamics Simulation of the Liquid-Metal−Amorphous-Semiconductor Transition in Germanium. *Phys. Rev. B* **1994**, *49*, No. 14251.
(43) Grimme, S.; Antony, J.; Ehrlich, S.; Krieg, H. A Consistent and Accurate Ab Initio Parametrization of Density Functional Dispersion Correction (DFT-D) for the 94 Elements H-Pu. *J. Chem. Phys.* **2010**, *132*, No. 154104.


https://dx.doi.org/10.1021/acscatal.0c03410
ACS Catal. XXXX, XXX, XXX−XXX

(44) Tougerti, A.; Methivier, C.; Cristol, S.; Tielens, F.; Che, M.; Carrier, X. Structure of Clean and Hydrated $\alpha$-$Al_2O_3$ (11 [Combining Macron] 02) Surfaces: Implication on Surface Charge. *Phys. Chem. Chem. Phys.* **2011**, *13*, 6531−6543.
(45) Henkelman, G.; Uberuaga, B. P.; Jónsson, H. A Climbing Image Nudged Elastic Band Method for Finding Saddle Points and Minimum Energy Paths. *J. Chem. Phys.* **2000**, *113*, 9901−9904.
(46) Yu, M.; Trinkle, D. R. Accurate and Efficient Algorithm for Bader Charge Integration. *J. Chem. Phys.* **2011**, *134*, No. 064111.


https://dx.doi.org/10.1021/acscatal.0c03410
*ACS Catal.* XXXX, XXX, XXX−XXX